

# Detectability of Nonlinear Gravitational Wave Memory

Darin C. Mumma<sup>1</sup>

Mentors: Alan J. Weinstein<sup>2</sup>, Colm Talbot<sup>2</sup>, and Alvin K. Y. Li<sup>2</sup>

<sup>1</sup>*Departments of Physics and Philosophy, Grove City College, Grove City, PA 16127, US and*

<sup>2</sup>*LIGO Laboratory, California Institute of Technology, Pasadena, CA 91125, US*

(Dated: July 31, 2020)

Gravitational waves passing through a region of spacetime leave behind a permanent distortion, with strain typically on the order of  $10^{-23}$ , the so-called memory effect. Linear and nonlinear components exist in gravitational wave memory, the latter appearing as a non-oscillatory, cumulative signal. Current gravitational wave detectors have not yet been able to reliably detect and isolate this low-frequency, nonlinear component which skews the numerical inferences of gravitational wave source parameters. Because this effect is cumulative, it is non-negligible, and its non-oscillatory nature distinguishes it from the rest of the waveform, making it detectable, in theory. Though previous studies have quantified and suggested improvements for the detectability of nonlinear memory, more templates and new data are available than ever before. In this project, we apply Bayesian parameter estimation to simulated gravitational waves from compact binary coalescences with memory to determine nonlinear memory detectability.

## I. INTRODUCTION

Although all accelerating masses radiate gravitational waves, compact binary coalescences – binary systems consisting of black holes and/or neutron stars – are especially interesting because they emit the most detectable gravitational wave signals and many of their properties are known[1–3]. Indeed, the amplitude and phase of a gravitational wave encodes source features such as mass, spin, and location[4]. A typical gravitational wave sourced from a compact binary coalescence is an oscillatory traveling wave with increasing frequency and momentary peak corresponding to the merger phase. As it propagates through spacetime, this waveform distorts surrounding mass arrangements in an oscillating pattern, but afterwards each arrangement returns to its original geometry. However, general relativity predicts that after a gravitational wave passes a truly free-falling arrangement of masses, a memory effect occurs in which a permanent nonzero difference in deformation is observable [5–7]. Further, all gravitational waves produce both linear and nonlinear memory.

Linear memory arises from non-oscillating masses and, thus, usually appears only in systems with hyperbolic orbits, neutrino ejection, or gamma-ray bursts [8]. Nonlinear memory arises from the signal contribution of secondary gravitational waves sourced by the initial wave emission. Unlike non-oscillating masses, secondary gravitational wave production occurs in many compact binary coalescences, making nonlinear memory especially prominent. Also, nonlinear memory accumulates over time because it is *hereditary* – depends on the entire past motion of the source. The non-oscillating and cumulative nature of nonlinear memory should, in theory, make it easy to distinguish from the primary component of a gravitational wave signal [9]. In practice this is not the case.

There is one reason why nonlinear memory is, in fact, hard to detect in a gravitational wave signal. As seen in Figure (1), the noise curves for the Livingston and Hanford detectors are minimized between 20–1000-Hz, the typical operating frequency of these detectors. However, nonlinear memory is all below this frequency band, where control and Poisson noise

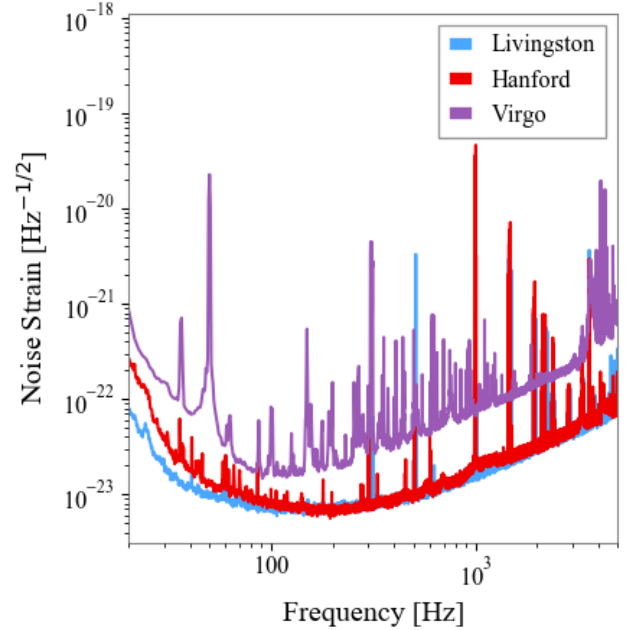


Figure 1. The noise curves for the LIGO Livingston, LIGO Hanford, and VIRGO detectors during the second observing run.

dominate. This has long been thought to lower the single-to-noise ratio (SNR) of the memory effect below the resolution of the detectors, rendering it undetectable.

Even in higher frequency bands detector data is very noisy. The primary goal of gravitational wave signal analysis is to distinguish actual signals from this background noise. All phases of compact binary coalescence-sourced waveforms are well-modeled using numerical simulations, allowing a template library to be constructed over a broad range of binary component masses and spins. Matched filtering can then be used to compare these templates with the data and determine the best fit. When nonlinear gravitational wave memory enters the picture, this same process can also be used to determine the detectability of the memory contribution by comparing the

memory component in the template with the observed signal in the detectors.

From here, we discuss the theoretical background behind gravitational waves, matched filtering, nonlinear memory, and parameter estimation in Section II. In Section III, we summarize the procedure involved in determining memory detectability. In Section IV, a progress update encompassing the first three weeks of the project is provided. Finally, Section V describes the work plan for the project.

## II. BACKGROUND

### A. Gravitational Wave Theory and Detection

An implication of Einstein's general relativity is that black holes, neutron stars, and other massive objects accelerating in spacetime generate traveling ripples known as gravitational waves [10]. Here we will discuss the speed and polarizations of gravitational waves as well as instruments and methods used to detect them.

#### 1. Speed of gravity

General relativity predicts that gravitational waves propagate at the speed of light,  $c$ , [10], and several measurements have been made to confirm this prediction using astrophysical observations. Most notably, Velten, Jimenez, and Piazza [11] used twenty-five years of orbital decay measurements for the Hulse-Taylor binary, and Abbott *et al* [12] used the difference in arrival time between GW170817 and GRB170817, both sourced from the same binary neutron star merger. The first experimenters were able to constrain gravity's speed to within 1% of  $c$  and the second were able to constrain it to within only  $10^{-13}\%$  of  $c$ .

#### 2. Gravitational wave polarizations and detectors

Another prediction of general relativity is that passing spacetime ripples distort an arrangement of test masses in an oscillatory manner. The frequency and amplitude of the oscillations are related to the angular momentum and mass of the ripple's source, respectively [4]. A Michelson-Morley interferometer may be used to record these variations in spacetime strain: two arms are set perpendicular to one another, and a laser and beamsplitter are arranged at the intersection point as shown in Figure (2). The laser is fired through the beamsplitter, creating two beams which travel along each arm and return after reflecting from mirrors placed at the end of each arm. Both beam paths are aligned to recombine at a photodiode located at the output port of the beamsplitter. Before a gravitational wave passes through, the only phase difference which exists between both beams arises from the difference in arm length, which is carefully adjusted to produce destructive interference at the photodiode.

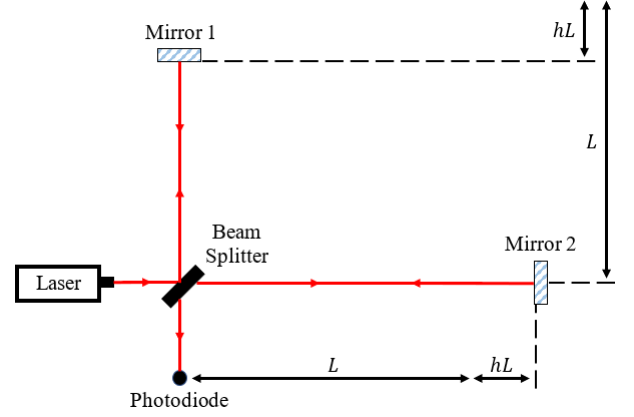


Figure 2. Simplified diagram of a standard LIGO detector. A gravitational wave traveling into the page is incident on the detector, changing each arm length by an amount  $hL$  ( $h$  is gravitational wave strain).

However, both arm lengths are changed oppositely to one another by a passing gravitational wave, altering the phase difference and, thus, combined intensity of the light incident on the photodiode. This intensity information may be translated to strain information which is given in Equation (1)

$$h_{ij}(t, \mathbf{r}) = \sum_{A=+, \times} e_{ij}^A(\hat{\mathbf{n}}) \int_{-\infty}^{+\infty} h_A(f) e^{-i2\pi f(t - \frac{\hat{\mathbf{n}} \cdot \mathbf{r}}{c})} df, \quad (1)$$

where  $h_{ij}$  is the strain tensor,  $\hat{\mathbf{n}}$  is the wave's propagation direction, and  $t - \frac{\hat{\mathbf{n}} \cdot \mathbf{r}}{c}$  is the retarded time tracking the wave's passage across the detector. In general relativity, the space-time metric is transverse-traceless gauge invariant, implying that free-falling test masses are at rest in spacetime. Although, the test masses (mirrors) in a given detector are supported by external forces, these are applied at low-frequencies (below 10 – 20-Hz), and are thus negligible at the operating frequencies of ground-based detectors. So, for these detectors, Equation (1) is independent of position  $\mathbf{r}$ , which may thus be set to 0 for a single detector (but will differ for other, non-co-located detectors). Recognizing the resulting integral as an inverse Fourier transform, this yields the expression given in Equation (2)

$$h_{ij}(t) = \sum_{A=+, \times} e_{ij}^A(\hat{\mathbf{n}}) h_A(t), \quad (2)$$

which clearly expresses the total strain as a sum of two polarization states,  $h_+$  (plus) and  $h_\times$  (cross). Both polarization states are transverse to the direction of propagation and are oriented  $45^\circ$  relative to one another as shown in Figure (3). Plus-polarized gravitational waves are a quarter-wave out of phase with cross-polarized gravitational waves, and, generally, incident gravitational waves are a linear combination of these two polarization states. Thus, gravitational waves may have linear, circular, or elliptical polarizations.

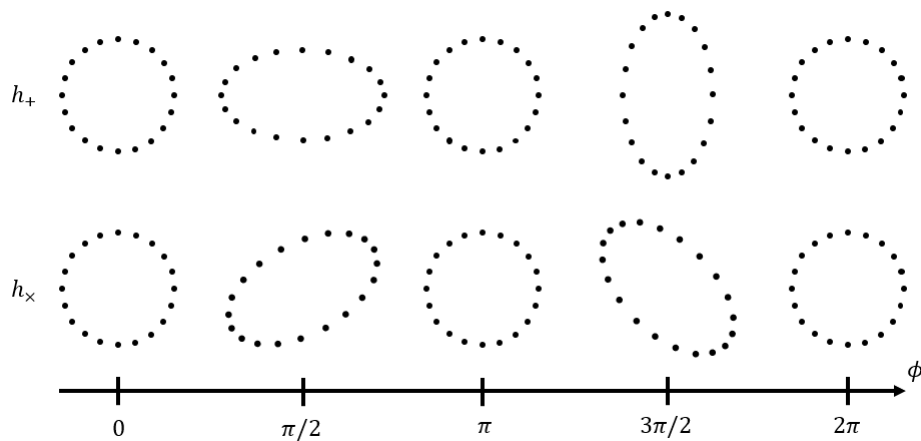


Figure 3. Linear polarizations of a gravitational wave illustrated over a complete phase cycle. Each dot represents a distinct test mass and the wave propagates into the plane of the paper.

### 3. Signal types and detection methods

To date, there are multiple, known gravitational wave types including continuous, stochastic, burst, and compact binary coalescence gravitational waves[13–15]. Continuous gravitational waves are radiated by spinning neutron stars and thus maintain constant frequency and amplitude. Stochastic gravitational waves likely come from especially distant sources and thus arrive from all directions, at all frequencies, and at all times. Burst gravitational waves have waveforms that are difficult to predict in advance but nevertheless exist as short duration pulses. Relevant to this paper, compact binary coalescence gravitational waves are sourced from inspiraling compact objects, such as black holes and/or neutron stars, and thus vary in frequency and amplitude over time. Compact binary coalescences consist of three phases, including an inspiral, merger, and ringdown as shown in Figure (4). In the inspiraling stage, the separation distance and orbital period of the binary components decay due to radiated energy in the form of gravitational waves. This portion of the signal increases in frequency and amplitude as the merger approaches. In the merger phase, the signal’s amplitude briefly peaks as the binary components combine. In the ringdown stage, the resulting merged black hole (or heavy neutron star) stabilizes, producing a signal with decreasing frequency and amplitude. Among these four types of gravitational waves, compact binary coalescence gravitational waves have the most well-modeled waveforms[1–3].

Increased detector sensitivity is achieved by equally extending both beam paths through the careful arrangement of mirrors which allow multiple reflections to take place before the beams are recombined. As a result, typical detector sensitivity allows for measurements of strain on the order of  $10^{-22}$ . However, this high sensitivity to spacetime strain makes it hard to distinguish between gravitational wave signals and background noise. This noise is often both local and non-local, frequently masking or even mimicking gravitational wave signals[16]. Random noise, such as quantum

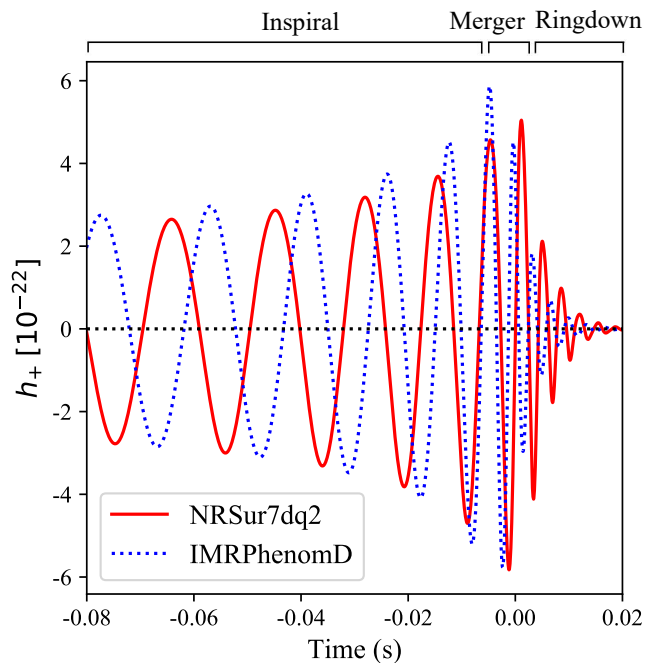


Figure 4. Compact binary coalescence gravitational-wave strain amplitude that shows the full bandwidth of a typical waveform. The inset labels indicate the inspiral, merger, and ringdown phases of two coalescing black holes.

and thermal noise, are often due to local causes and is thus uncorrelated among an array of distant detectors, whereas a passing gravitational wave is incident on every point of the earth nearly simultaneously. So, using the *coincidence criterion*, comparison of data among multiple detectors may be used to distinguish real signals from random signals. The coincidence criterion may also be used to identify non-local noise such as earthquakes and other seismic waves (i.e. those caused by ocean waves colliding with the continental plates).

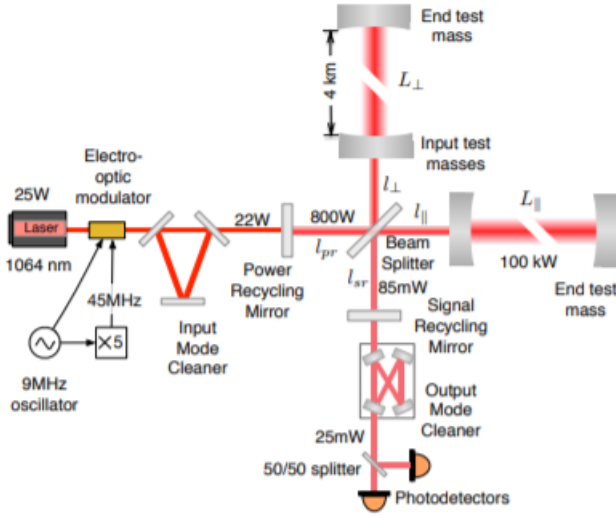


Figure 5. More detailed diagram of a standard LIGO detector. The annotations show the optical power in use during the first LIGO observing run. These power levels are a factor of  $\sim 8$  smaller compared to the designed power levels. The Nd:YAG laser, with wavelength  $\lambda = 1064\text{-nm}$ , is capable of producing up to 120-W, but only 22-W were used. A suspended, triangular Fabry-Perot cavity serves as an input mode cleaner to clean up the spatial profile of the laser beam, suppress input beam jitter, clean polarization, and to help stabilize the laser frequency. The Michelson interferometer is enhanced by two 4-km-long resonant arm cavities, which increase the optical power in the arms by approximately a factor of 270. Since the Michelson interferometer is operated near complete destructive interference, all but a small fraction of the light is directed back towards the laser. The power recycling mirror resonates this light again to increase the power incident on the beamsplitter by a factor of nearly 40, improving the quantum Poisson noise sensing limit and filtering laser noises. On the anti-symmetric side, the signal recycling mirror is used to broaden the response of the detector beyond the linewidth of the arm cavities. An output mode cleaner is present at the antisymmetric port, to reject unwanted spatial and frequency components of the light, before the signal is detected by the main photodetectors. Retrieved from Martynov *et al* [17].

During periods of low seismic activity, gravitational wave candidates may still be trusted; however, during periods of intense seismic activity, any gravitational wave candidate is often untrustworthy and may be rejected outright. Methods to reduce noise and increase detector sensitivity is shown in Figure (5). Identifying gravitational waves is further improved by comparing data to numerical templates constructed according to general relativity. This process, known as matched filtering, is explained in the next section.

## B. Matched Filtering

Matched filtering plays an important role in identifying gravitational waves and determining memory detectability through parameter estimation. Here we will start by describing matched filtering without memory and then include memory afterwards.

### 1. Matched filtering without memory

The ability to extract a signal from background noise is given by the SNR,  $\rho$ , which is typically low, and matched filtering is a process by which it may be increased[18]. In matched filtering, gravitational wave templates are cross-correlated with observed data in the frequency domain by sliding template waveforms along the data until a maximum correlation value is reached. However, the presence of non-Gaussian noise (glitches) in the data makes a direct application of this process impossible, requiring us to introduce a filter kernel  $\tilde{K}(f)$  which is related to the template in some unknown way.

First, the correlation value,  $\hat{s}$ , is related to the strength of the signal,  $\langle S \rangle$ , according to Equation (3)

$$\begin{aligned} \langle S \rangle &= \langle \hat{s} \rangle = \int \langle \tilde{s}(f) \tilde{K}(f) \rangle df \\ &= \int \tilde{h}(f) \tilde{K}^*(f) df, \end{aligned} \quad (3)$$

where  $\tilde{s}(f) = \tilde{h}(f) + \tilde{n}(f)$  is the data in the frequency domain,  $\tilde{h}(f)$  is the template's waveform,  $\tilde{n}(f)$  is the background noise, and  $\tilde{K}(f)$  is the filter function. The second line is obtained by applying Parseval's Theorem and assuming  $\tilde{n}(f)$  is Gaussian (random), making  $\langle \tilde{n}(f) \tilde{K}(f) \rangle = 0$ .

Second, let the one-sided power spectral density of the data's noise,  $S_n(f)$ , be defined as  $\langle |\tilde{n}(f)|^2 \rangle$ . Then, if no signal is present,  $\tilde{h}(f) = 0$  and the root mean square of the noise,  $N$ , is given by

$$\begin{aligned} N &= \sqrt{\langle \hat{s}^2 \rangle - \langle \hat{s} \rangle^2} \Big|_{\tilde{h}=0} \\ &= \sqrt{\int \langle \hat{s}^2 \rangle df} \\ &= \sqrt{\int \langle \tilde{n}(f) \tilde{n}(f') \rangle \tilde{K}(f) \tilde{K}(f') df df'} \\ &= \sqrt{\frac{1}{2} \int S_n(f) |\tilde{K}(f)|^2 df}. \end{aligned} \quad (4)$$

Thus,  $\rho = \frac{\langle S \rangle}{N}$  may be written as

$$\rho = \frac{\int \tilde{h}(f) \tilde{K}^*(f) df}{\sqrt{\frac{1}{2} \int S_n(f) |\tilde{K}(f)|^2 df}}, \quad (5)$$

or, defining the inner product between  $\tilde{x}$  and  $\tilde{y}$  as

$$\langle \tilde{x}, \tilde{y} \rangle = \mathbb{R} \left( \int \frac{\tilde{x}(f)\tilde{y}(f)}{\frac{1}{2}S_n(f)} df \right), \quad (6)$$

$\rho$  can be simplified, yielding

$$\rho = \frac{\langle \frac{1}{2}S_n\tilde{K}, \tilde{h} \rangle}{\sqrt{\langle \tilde{h}, \tilde{h} \rangle}}. \quad (7)$$

It is readily seen that Equation (7) is maximized when  $S_n\tilde{K} \propto \hat{h}$ , or, equivalently, when

$$\tilde{K}(f) \propto \frac{\tilde{h}(f)}{S_n(f)}. \quad (8)$$

If we redefine  $\rho$  as the frequency series,  $S/N$ , and combine Equations (3) and (8), we have

$$\rho = \frac{1}{N} \int \frac{\tilde{s}(f)}{S_n(f)} \tilde{h}(f) df, \quad (9)$$

from which we can see that  $\tilde{K}(f)$  has the effect of dampening glitch frequencies, allowing signal frequencies to be heard more easily.

Equation (9) tells us that we must first whiten the data by dividing out  $S_n(f)$  and, afterward, cross-correlate the whitened data with a template which matches the signal as closely as possible. The result is interpreted as an SNR time series which only achieves large values if a signal is present and agrees closely with the template.

Matched filtering can be completed for a network of detectors with the result given in Equation (10)

$$\rho_{net} = \sqrt{\sum_i \rho_i^2}, \quad (10)$$

where  $i$  runs over each detector and  $\rho_{net}$  is referred to as the network SNR ratio. Typically, signal must have  $\rho_{net} > 8$  to be detected, but both signals and glitches can satisfy this requirement, introducing the significant possibility of false detection. We can drastically reduce the likelihood of false detection by requiring each  $\rho_i$  to be above a certain threshold: the coincidence criterion mentioned above.

## 2. Matched filtering with memory

Matched filtering can also be used to determine the detectability of the memory contribution. If the output of the matched filter using a template containing memory yields a significantly higher SNR ratio from the data than the output using a template without memory, the ability to detect memory is likely. The mathematical details involve parameter es-

timation and computation of a Bayes' factor, which will be explained after a discussion of nonlinear memory.

## C. Nonlinear Memory Theory

The nonlinear (Christodoulou) gravitational wave memory is a permanent strain in spacetime due to the passage of gravitational waves [8, 9]. According to general relativity, a post-Newtonian expansion exists in which nonlinear memory is described by terms which immediately follow the primary waveform and linear memory. However, far from being negligible, these terms accumulate memory over the duration of the signal, increasing most rapidly during the merger as seen in Figure (6). These increasing terms arise from the signal contribution of secondary gravitational waves sourced by the primary waveform, and can thus be viewed as linear memory from waves which began from an arbitrary point in spacetime. Nonlinear memory is shown in Figure (7) for a plus polarized signal. The non-linear component is readily seen to be substantial.

The strength of nonlinear memory depends on incident angle in much the same way as the primary waveform and, as just mentioned, increases monotonically over time. It is clear, then, that nonlinear memory has an angular and temporal dependence which vary independent of one another, suggesting separation of variables. Indeed, through an application of separation of variables and projection of the linear polarizations of the waveform onto the spherical harmonics, one yields

$$\delta h_{lm} = \frac{R}{4\pi c} \Gamma_{lm}^{l_1 l_2 m_1 m_2}(\Omega) H_{l_1 l_2 m_1 m_2}(T_0, T_F), \quad (11)$$

where  $l$  and  $m$  designate a spherical harmonic mode for each binary component,  $\delta h_{lm}$  is the overall non-linear memory for a given mode,  $\Gamma_{lm}^{l_1 l_2 m_1 m_2}(\Omega)$  encodes the angular dependence of the memory, and  $H_{l_1 l_2 m_1 m_2}(T_0, T_F)$  encodes the time dependence.  $\Gamma_{lm}^{l_1 l_2 m_1 m_2}(\Omega)$  is a geometry factor closely related to the spherical harmonics and may thus be tabulated and inserted in advance before any experiment-specific calculations are made.  $H_{l_1 l_2 m_1 m_2}(T_0, T_F)$  is closely related to the total intensity of the secondary waveforms and thus must be computed after each signal is collected and processed. Using Equation (11), a tabulation of the spherical harmonics, and a properly chosen region of interest in an incident signal, nonlinear memory may be calculated.

Accurate identification and measurement of nonlinear memory will allow comparison with models, potentially lending further support to general relativity. Also, this will allow nonlinear memory to be extracted from gravitational waveforms which will increase the accuracy of source parameter measurements. With the recent conclusion of the third LIGO observing run, much current data is now available, allowing for the detectability of non-linear memory to be determined. From such a determination, the magnitude and nature of sensitivity improvements for each detector may be evaluated so non-linear memory can be effectively detected in future observing runs.

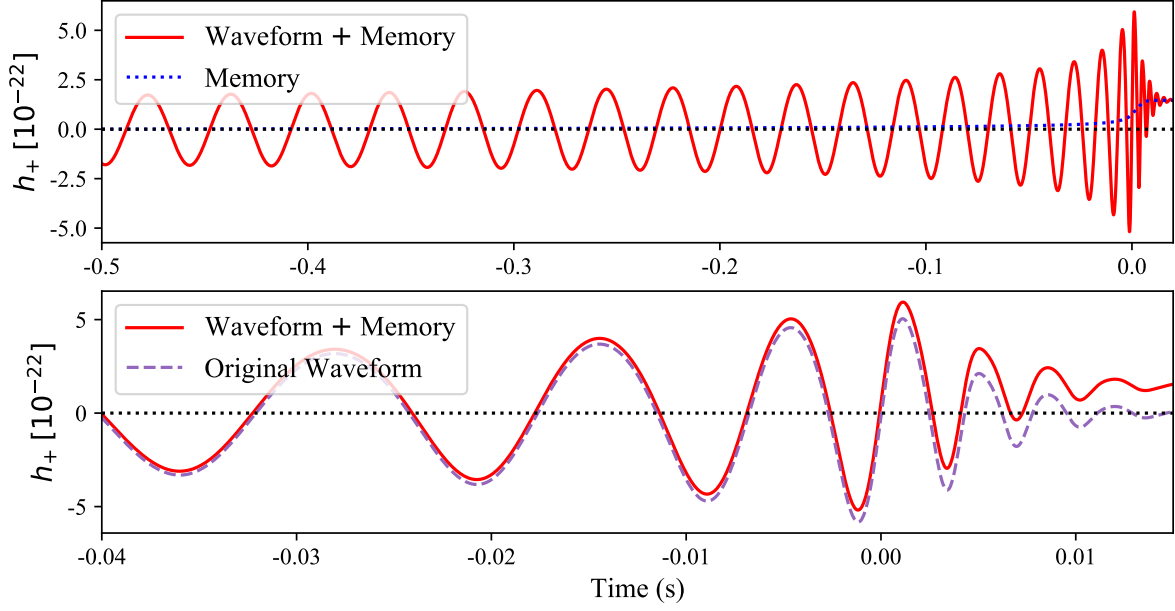


Figure 6. An example of a plus-polarized gravitational waveform with memory. The waveform approximant used is NRSur7dq2 and the source parameters include a total mass of  $60M_{\odot}$ , mass ratio of 2, and 0 spin for both components. (TOP) Inclusion of early inspiraling shows that most memory accumulates during the merger phase. (BOTTOM) Excluded inspiral stage with superposed waveforms, with and without memory, to illustrate the memory effect on waveforms.

#### D. Bayesian Parameter Estimation

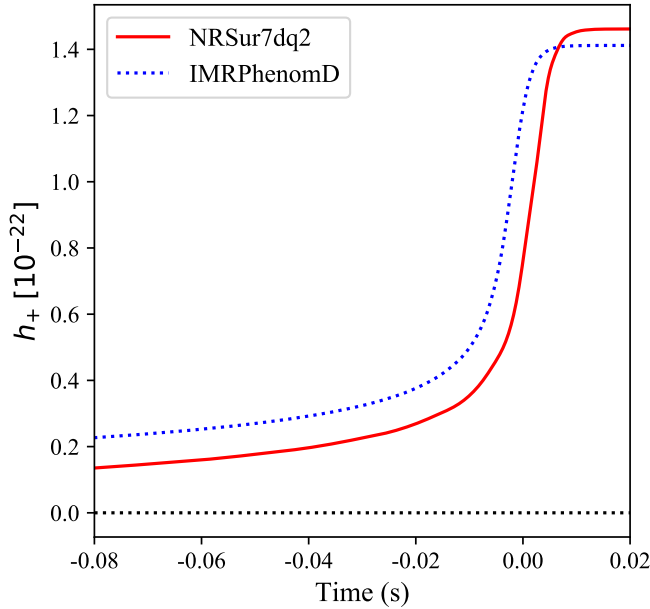


Figure 7. Superposed memory plots using two different approximants, nonspinning components, a total mass of  $60M_{\odot}$ , and a mass ratio of 2. Differences in time of accumulation and final memory exist and can be significant based on source parameters.

Let the hypothesis  $H$  be the statement, “non-linear memory is present in the detector’s data” and, further, let  $D$  be the detectors’ data. Then,  $P(H | D)$  is the probability that nonlinear memory is present in the data given the data we have at hand,  $P(D | H)$  is the likelihood that we will detect nonlinear memory given that nonlinear memory is, in fact, present,  $P(H)$  is the belief we have in the presence of nonlinear memory on the basis of prior information (or lack of information) alone, and  $P(D)$  is the evidence offered by the data independent of the hypothesis under consideration. Bayes’ Theorem relates these four quantities as shown in Equation (12).

$$P(H | D) = \frac{P(D | H) \times P(H)}{P(D)} \quad (12)$$

Equation (12) is used in Bayesian inferencing to update  $P(H | D)$  as more data becomes available, and we would like to satisfy Equation (12) by determining  $P(H | D)$  and  $P(\sim H | D)$  and computing the associated posterior odds. This process may be used to estimate pre-known parameter values and reasonable, or even improved, estimations with memory included in the model indicates a high likelihood of memory detectability.

The first step in parameter estimation is to present  $H$  as in Equation (13)



$$h_{\text{tot}} = h + \lambda h_{\text{mem}}, \quad (13)$$

where  $h_{\text{tot}}$  is the total signal,  $h$  is the non-memory portion of the signal, and  $h_{\text{mem}}$  is nonlinear memory. Then, for the injected template with known memory,  $\lambda = 1$  but for the purposes of parameter estimation can take on any value. A posterior distribution for  $\lambda$  consistent with a value of 1 indicates a high likelihood of memory detection.

### III. PROCEDURE

In this project, we will assess the detectability of memory in gravitational waves and subsequently search for methods to improve it. To achieve this goal, sufficient mastery of Bayesian parameter estimation, signal simulation, and python coding must be achieved. Here we will discuss the projected stages of the project.

Firstly, I will become familiar with python and PyCBC [19, 20], a python package containing algorithms that can detect coalescing compact binaries and measure gravitational wave parameters. General python competency will equip me with the required coding skills which will be necessary later in the project while PyCBC will acquaint me with the general shape of gravitational waveforms and how to generate them.

Secondly, I will become familiar with the python package GWmemory [21], which calculates and constructs nonlinear memory waveforms from selected gravitational signals. Familiarity with this package will improve my understanding of memory effects on gravity wave signals and how to generate signals with memory.

Third, I will acquire a better understanding of Bayesian inference and become familiar with BILBY [22, 23], a python package which consists of inferencing tools for parameter estimation.

Fourthly, we will work on our primary goal by assessing the detectability of memory in gravitational waves. Equation (13) presents an all-or-nothing waveform model for templates, where  $\lambda$  represents the memory constant. We will superpose a signal with memory (i.e.  $\lambda = 1$ ) on a typical noise distribution, and then apply matched filtering to measure the signal and infer the value of the memory constant. This inferred value represents the memory detectability, and a value close to 1 means we are likely able to identify memory in a given signal.

Fifthly, given additional time, we will investigate methods by which the detectability of gravitational wave memory can be improved.

### IV. PROGRESS UPDATE

Here we will briefly outline progress made on the project, current objectives, and future plans with expected challenges.

#### A. Completed objectives

I attended SURF lectures on gravitational wave theory, noise and signal patterns, Bayesian inferencing, and detector geometry. I also completed work on tutorials involving written work and programming, which covered simulation of gravitational waves through frequency vs. time plots and in the time and frequency domains. Transformation of signals between the time and frequency domains and worked examples of the matched filtering process were also included. Texts on Bayesian inferencing and practice with parameter estimation using various models, prior restrictions, and samplers improved my application ability and understanding of Bayes' rule. Because I used PyCBC and BILBY to complete many of these tutorials, I also acquired familiarity with these programs. Figures (1) and (4) show noise curves and waveforms that I generated using the knowledge I acquired.

Multiparameter estimation takes a long time to execute and, thus, preparations were made to work on the LIGO computing cluster. I installed a Linux virtual machine with python fully configured. BILBY, PyCBC, and GWMemory were then downloaded and installed. From here on, programs were written using VIM [24] to transition easily to the computing cluster later in the project. Subsequent programs included plots made with GWMemory to familiarize the primary author with memory plots in the frequency and time domains. Several of these plots are given in Figures (6), (7), and (8).

File transfer and program collaboration has been facilitated through a GitHub repository and, in the future, through the computing cluster. I have since learned to add and adjust entries in the repository and am learning to do so in the cluster.

Before moving into the Bayesian approach to parameter estimation, I began with a frequentist approach which handles 1- and 2-dimensional parameter estimation more efficiently than the Bayesian approach, but can only do so correctly for Gaussian likelihoods (which is true of LIGO and Virgo data to first order) since priors do not exist in frequentist statistics. In the frequentist approach, the location in parameter space for which a statistical index,  $\chi^2$ , is at a minimum marks the most likely values for each inferred parameter. The link between  $\chi^2$  and likelihood is given in Equation (14)

$$\log(P(D_i, f_i | \lambda, H)) = -\frac{1}{2} \left[ \sum_{i=1}^n \frac{|D_i - (h_i + \lambda h_{\text{mem}})|^2}{\sigma_i^2} + 2\log(2\pi\sigma^2) \right], \quad (14)$$

where  $P(D_i, f_i | \lambda, H)$  is the likelihood associated with the data,  $D_i$ , and frequencies,  $f_i$ , given  $\lambda$  and the hypothesis,  $H$ , that memory exists in the signal.  $\chi^2$  is the summation term on the right hand side of the equation. Clearly, if the goal is to find the location in parameter space for which  $\chi^2$  is at a minimum, then we could accomplish this goal by finding the location at which the likelihood is at a maximum. Figures (9) and (10) illustrate this approach graphically and analytically.

Finally, we have completed our BILBY parameter estimation code which features a gravitational wave model with

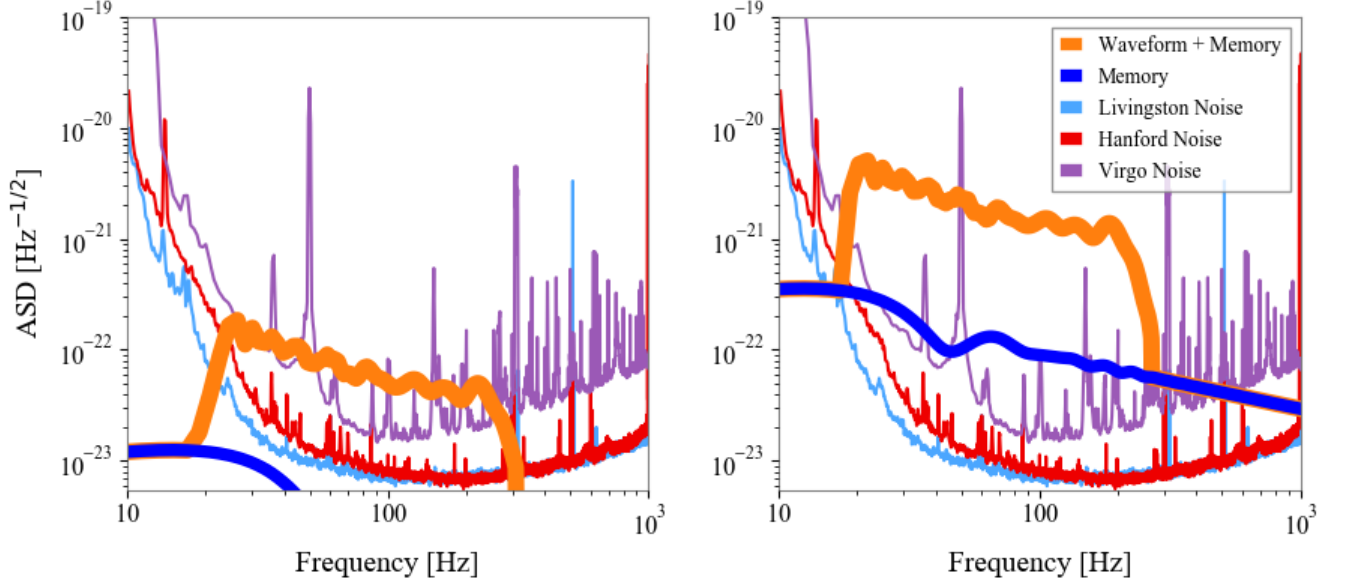


Figure 8. Waveforms in the frequency domain superposed with noise curves from the second observing run. It should be noted that the oscillatory waveform is generated from 20-Hz upward and is thus incorrect below this frequency. Since the memory contributed by a 20-Hz signal exists at far lower frequencies, the memory is correct over each of these plot’s domain, and clearly shows dominant power at sub-20-Hz frequencies. (LEFT) Source parameters are those of GW150914. Here, the predicted nonlinear memory (blue) cannot be detected in the data. (RIGHT) Both components are nonspinning with total mass =  $80M_{\odot}$ , mass ratio = 1, and luminosity distance = 20Mpc. If a signal sourced from a system with these parameters were incident on the detectors, the accompanying memory would likely be detectable.

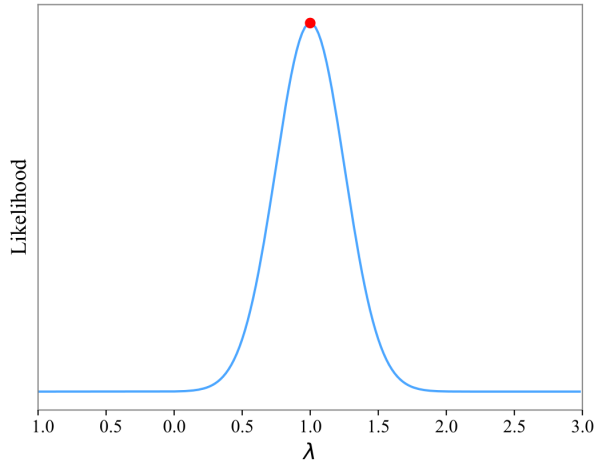


Figure 9. The injected waveform used to generate this likelihood distribution is sourced by non-spinning components with  $M_{\text{tot}} = 60M_{\odot}$ ,  $q = 1$ ,  $d_L = 100$  Mpc,  $\iota = \pi/2$ ,  $\psi = 0$ ,  $\phi = 0$ ,  $\alpha = 0$ ,  $\delta = 0$ . The red dot is the peak value and location computed through `scipy.optimize`.

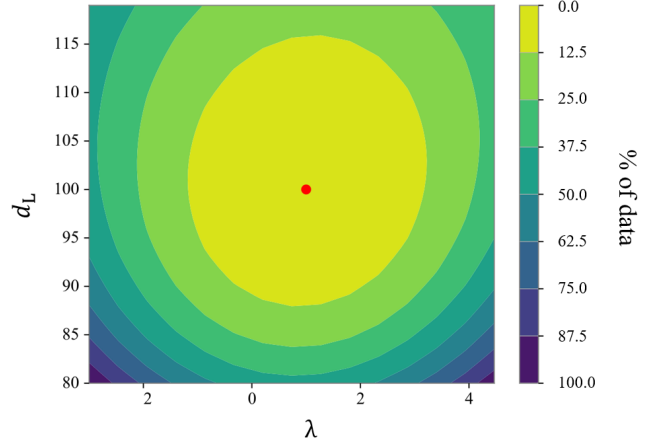


Figure 10. The injected waveform used to generate this likelihood distribution is sourced by non-spinning components with  $M_{\text{tot}} = 60M_{\odot}$ ,  $q = 1$ ,  $d_L = 100$  Mpc,  $\iota = \pi/2$ ,  $\psi = 0$ ,  $\phi = 0$ ,  $\alpha = 0$ ,  $\delta = 0$ . The red dot is the peak value and location computed through `scipy.optimize`.

memory and uniform priors for all inferred parameters. In the end, we want to use this code to determine the LIGO and VIRGO detectors’ capability for identifying nonlinear memory. An outline of our process is given in Figure (11). Thus far, we have only examined simulated data with high SNR ( $\approx 1000$ ) to debug the code, run simple experiments, and observe output effects when settings are varied. Figures (12) - (15) show sample corner plots for 1-, 2-, and 3-dimensional

parameter estimation. In all cases, the high SNR allows for accurate parameter estimation, yet the lingering PSD still allows for differences in standard deviation between posterior distributions when, say, distance is varied. In all 1-dimensional probability distribution functions (PDFs), the orange vertical line demarcates the given parameter’s actual value and the dotted, blue, vertical lines subtend the  $2\sigma$  confidence interval. In all 2-dimensional contour plots, the three regions in order of



decreasing brightness are the  $1\sigma$ ,  $2\sigma$ , and  $3\sigma$  regions.

## B. Current objectives

Lasky, et al. [25] predicts that a double degeneracy exists for the  $(2,2)$  mode in polarization angle,  $\psi$ , and phase,  $\phi$ , which leads to a bimodal distribution for  $\lambda$ . This bimodality arises because a  $(2,2)$ -only oscillatory waveform with parameters  $(\psi, \phi)$  is unchanged by the transformation  $(\psi + 2\pi, \phi + 2\pi)$ , but, under the same transformation, the memory constant changes sign. Including higher order modes breaks the degeneracy. Using Bayesian parameter estimation, we empirically prove this effect as shown in Figure (16).

## C. Future plans and expected challenges

Next, we will find the distance at which  $\lambda$ 's one-dimensional PDF's bimodality can be resolved as in the left plot in Figure (16). Also, we intend to make the NRSur7dq4 approximant compatible with GWMemory which will allow us to extend the mass ratio,  $q$ , limit from 2 to 4 and is becoming more important as higher mass ratio binaries are being discovered [26]. Also, we would like to increase the dimensionality of our parameter space and reduce the datas' SNR to realistic levels.

Inferring more than three parameters and adding noise will present a serious challenge. The full parameter space for a binary black hole contains fifteen dimensions, and we intend to add a sixteenth with the memory constant. This makes a single BILBY iteration take on the order of a second. But, in addition, we plan to determine the region of interest in the parameter space over which memory is detectable. This requires execution of the BILBY program for each choice of prior, leading to billions of iterations. Thus, a brute force approach which likely take *far* too long to complete. Early solutions include reducing the parameter space, accelerating the process through parallel computing, and submitting scripts through the LIGO computing cluster. Because the memory effect is most sensitive to changes in chirp mass, mass ratio, and component spins, the reduced parameter space will likely consist of these, and such a reduction will be trivial to put into practice. The second solution may not be completeable during this project; however, we will certainly try. The third solution requires familiarity with directed acyclic graph (DAG) files and parser arguments, both of which I will focus on next.

## V. WORK PLAN

A work plan has been included in Table I, listing weekly project goals for the Summer 2020 LIGO SURF project.

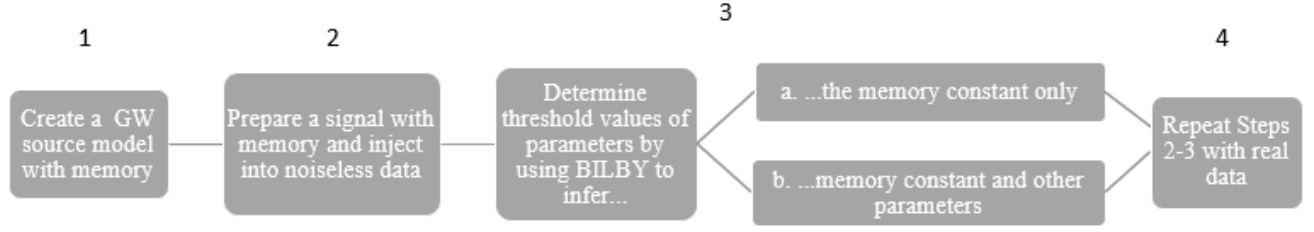


Figure 11. Flow chart which outlines our inferring process.

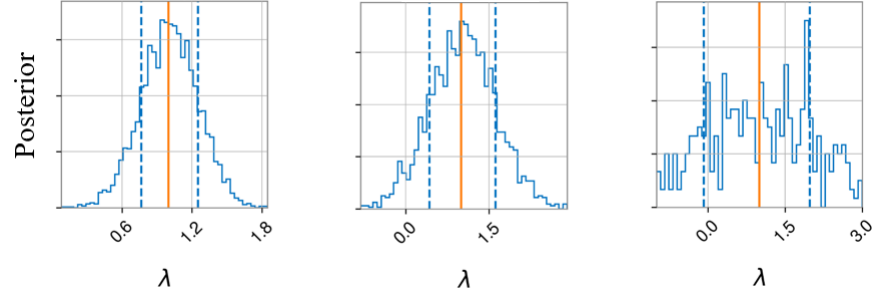


Figure 12. Standard deviation increases with distance, indicating that the data gives diminishing information for how to great the prior. The injected waveform used to generate each plot is sourced by non-spinning components with  $M_{\text{tot}} = 60M_{\odot}$ ,  $q = 1.5$ ,  $\iota = \pi/2$ ,  $\psi = 0$ ,  $\phi = 0$ ,  $\alpha = 0$ ,  $\delta = 0$ . (Left)  $d_L = 100$  Mpc, (Center)  $d_L = 500$  Mpc, and (Right)  $d_L = 1000$  Mpc.

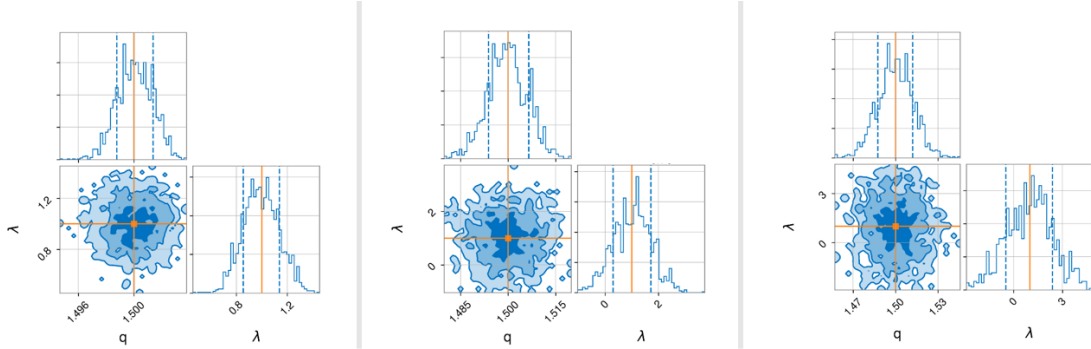


Figure 13. Both  $q$  and  $\lambda$ 's PDF widen with distance. The scales indicate that, unsurprisingly,  $q$ , is measured more accurately than  $\lambda$  at each distance. The injected waveform used to generate each plot is sourced by non-spinning components with  $M_{\text{tot}} = 60M_{\odot}$ ,  $q = 1.5$ ,  $\iota = \pi/2$ ,  $\psi = 0$ ,  $\phi = 0$ ,  $\alpha = 0$ ,  $\delta = 0$ . (Left)  $d_L = 100$  Mpc, (Center)  $d_L = 500$  Mpc, and (Right)  $d_L = 1000$  Mpc.

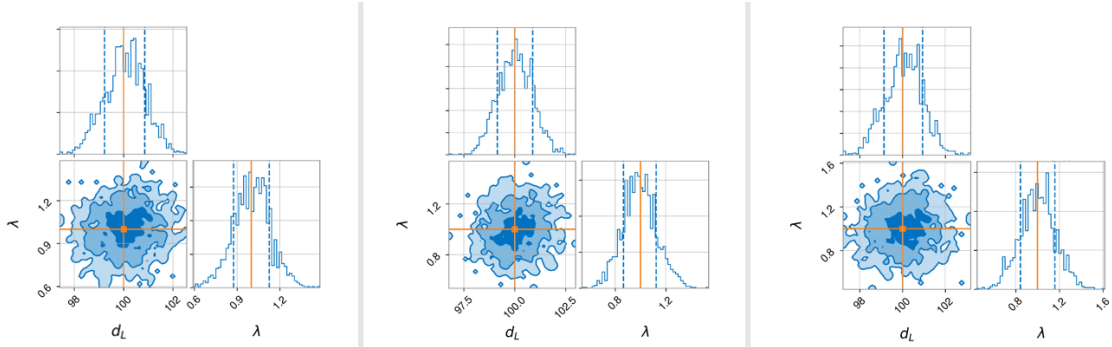


Figure 14.  $d_L$ 's posterior remains unchanged for each  $q$  value, but  $\lambda$ 's posterior increases in width for increasing  $q$ . The injected waveform used to generate each plot is sourced by non-spinning components with  $M_{\text{tot}} = 60M_{\odot}$ ,  $d_L = 100$  Mpc,  $\iota = \pi/2$ ,  $\psi = 0$ ,  $\phi = 0$ ,  $\alpha = 0$ ,  $\delta = 0$ . (Left)  $q = 1$ , (Center)  $q = 1.5$ , and (Right)  $q = 2$ .

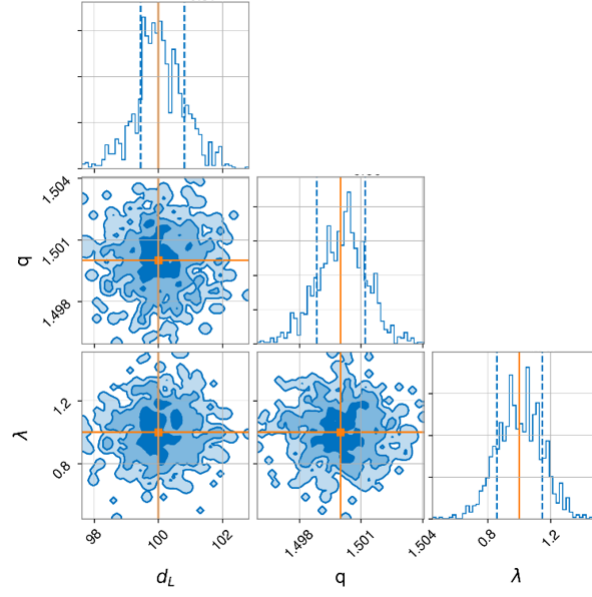


Figure 15. 3-dimensional parameter estimation for  $d_L$ ,  $q$ , and  $\lambda$ . The injected waveform used to generate each plot is sourced by non-spinning components with  $M_{\text{tot}} = 60M_{\odot}$ ,  $q = 1.5$ ,  $d_L = 100$  Mpc,  $\iota = \pi/2$ ,  $\psi = 0$ ,  $\phi = 0$ ,  $\alpha = 0$ ,  $\delta = 0$ .

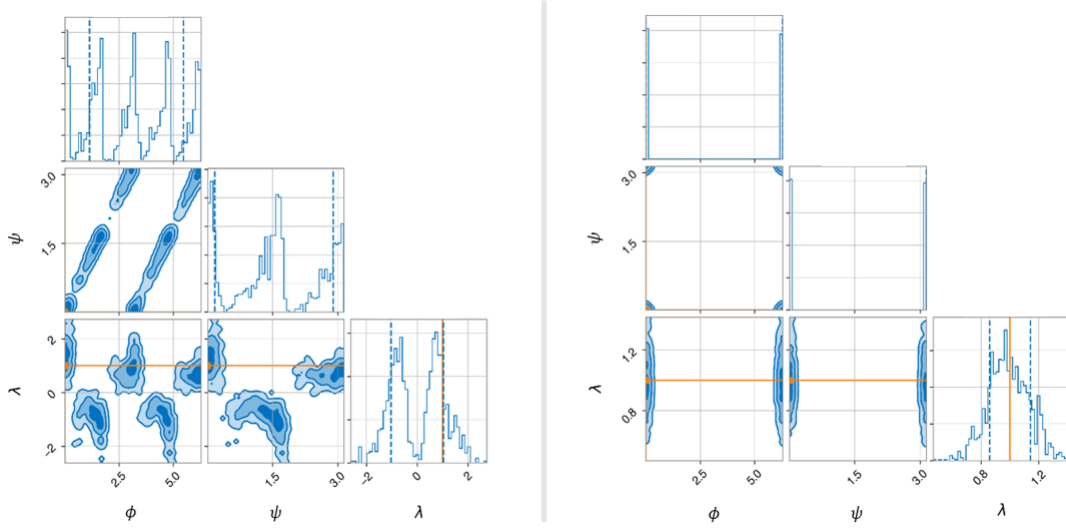


Figure 16. (*Left*) Inferring  $\psi$ ,  $\phi$ , and  $\lambda$  for a  $(2, 2)$  mode-only injected signal introduces bimodality in  $\lambda$ 's PDF. (*Right*) The bimodality is absent when higher order modes are introduced. The injected waveform used to generate each plot is sourced by non-spinning components with  $M_{\text{tot}} = 60M_{\odot}$ ,  $q = 1.5$ ,  $d_L = 100$  Mpc,  $\iota = \pi/2$ ,  $\psi = 0$ ,  $\phi = 0$ ,  $\alpha = 0$ ,  $\delta = 0$ .

Table I. Work plan for the Summer 2020 LIGO SURF program. Schedule is broken down by week and projected progress.

Date	Progress
June 1	1. Deadline for submitting project proposal.
June 16	2. Start of LIGO SURF 2020.
June 16–20 (Week 1)	3. Understand basic python and PyCBC, and BILBY functionality.
June 21–27 (Week 2)	4. Increase ability to work with PyCBC and BILBY.
July 28–July 4 (Week 3)	5. Familiarize with GWmemory.
July 5–11 (Week 4)	6. Investigate frequency domain memory and BILBY memory model. 7. Submit interim report 1.
July 12–18 (Week 5)	8. Main Project: Formation of effective work flow.
July 19–25 (Week 6)	9. Start main project.
July 26–August 1 (Week 7)	11. Submit interim report 2. 12. Submit abstract.
August 2–8 (Week 8)	13. Main Project: Produce results.
August 9–15 (Week 9)	14. Investigate detectability improvement.
August 16–21 (Week 10)	15. Continue investigating detectability improvement. 16. Final presentation.
September 28	17. Deadline for submitting final report.

- 
- [1] F. Pretorius. *Phys. Rev. Lett.*, 95(12), 2005.  
[2] M. Campanelli et al. *Phys. Rev. Lett.*, 96(11), 2006.  
[3] J. G. Baker et al. *Phys. Rev. Lett.*, 96(11), 2006.  
[4] B. P. Abbott et al. *Phys. Rev. X*, 9(3), 2019.  
[5] Y. B. Zeldovich and A. G. Polnarev. *Sov. Astron.*, 18(17), 1974.  
[6] V. B. Braginsky and L. P. Grishchuk. *Sov. Phys. JETP*, 62(3): 427–430, 1985.  
[7] V. B. Braginsky and K. S. Thorne. *Nature*, 327(6118):123–125, 1987.  
[8] Kip S. Thorne. *Phys. Rev. D*, 45(2):520–524, 1992.  
[9] M. Favata. *Classical Quantum Gravity*, 27(8), 2010.  
[10] A. Einstein. *Sitzungsber. Preuss. Akad. Wiss.*, 1:135–149, 1918.  
[11] Hermano Velten, Jose Beltran Jimenez, and Federico Piazza. *International Journal of Modern Physics: Conference Series*, 45, 2017.  
[12] B. P. Abbott et al. *The Astrophysical Journal*, 848(2):L13, 2017.  
[13] S. Klimenko et al. *Phys. Rev. D*, 93, 2016.  
[14] N. Christensen. *Rept. Prog. Phys.*, 82(1), 2018.  
[15] M. A. Papa et al. *ApJ*, 897(1), 2020.  
[16] S. Mukherjee et al. *Phys. Conf. Ser.*, 243, 2010.  
[17] D. V. Martynov et al. *Physical Review D*, 93(11), 2016.  
[18] H. Gabbard et al. *Phys. Rev. Lett.*, 120, 2017.  
[19] [iopscience.iop.org/article/10.1088/0264-9381/33/21/215004/meta](https://iopscience.iop.org/article/10.1088/0264-9381/33/21/215004/meta), .  
[20] [www.pycbc.org](http://www.pycbc.org), .  
[21] [github.com/colmtalbot/gwmemory](https://github.com/colmtalbot/gwmemory).  
[22] [lscsoft.docs.ligo.org/bilby/index.html](https://lscsoft.docs.ligo.org/bilby/index.html).  
[23] [arxiv.org/abs/1811.02042](https://arxiv.org/abs/1811.02042).  
[24] [www.vim.org](http://www.vim.org).  
[25] P. D. Lasky et al. *Phys. Rev. Lett.*, 117, 2016.  
[26] R. Abbott et al. *Astrophys. J. Lett.*, 896(2), 2020.